# Determination of the Partial Reactions of Rotational Catalysis in $F_1$-ATPase†

Joanne A. Baylis Scanlon, Marwan K. Al-Shawi, Nga Phi Le,‡ and Robert K. Nakamoto*

*Department of Molecular Physiology and Biological Physics, University of Virginia, P.O. Box 800736, Charlottesville, Virginia 22908-0736*

*Received March 30, 2007; Revised Manuscript Received May 3, 2007*

ABSTRACT: Steady-state ATP hydrolysis in the $F_1$-ATPase of the $F_OF_1$ ATP synthase complex involves rotation of the central $\gamma$ subunit relative to the catalytic sites in the $\alpha_3\beta_3$ pseudo-hexamer. To understand the relationship between the catalytic mechanism and $\gamma$ subunit rotation, the pre-steady-state kinetics of Mg·ATP hydrolysis in the soluble $F_1$-ATPase upon rapid filling of all three catalytic sites was determined. The experimentally accessible partial reactions leading up to the rate-limiting step and continuing through to the steady-state mode were obtained for the first time. The burst kinetics and steady-state hydrolysis for a range of Mg·ATP concentrations provide adequate constraints for a unique minimal kinetic model that can fit all the data and satisfy extensive sensitivity tests. Significantly, the fits show that the ratio of the rates of ATP hydrolysis and synthesis is close to unity even in the steady-state mode of hydrolysis. Furthermore, the rate of Pi binding in the absence of the membranous $F_O$ sector is insignificant; thus, productive Pi binding does not occur without the influence of a proton motive force. In addition to the minimal steps of ATP binding, reversible ATP hydrolysis/synthesis, and the release of product Pi and ADP, one additional rate-limiting step is required to fit the burst kinetics. On the basis of the testing of all possible minimal kinetic models, this step must follow hydrolysis and precede Pi release in order to explain burst kinetics. Consistent with the single molecule analysis of Yasuda et al. (Yasuda, R., Noji, H., Yoshida, M., Kinosita, K., and Itoh, H. (2001) *Nature* 410, 898−904), we propose that the rate-limiting step involves a partial rotation of the $\gamma$ subunit; hence, we name this step $k_\gamma$. Moreover, the only model that is consistent with our data and many other observations in the literature suggests that reversible hydrolysis/synthesis can only occur in the active site of the $\beta_{TP}$ conformer (Abrahams, J. P., Leslie, A. G. W., Lutter, R., and Walker, J. E. (1994) *Nature 370,* 621−628).

Steady-state ATP hydrolysis in the $F_1$-ATPase involves rotation of the central $\gamma$ subunit relative to the catalytic sites in the $\alpha_3\beta_3$ pseudo-hexamer (see refs *1*−*7* for reviews). At any point in time, the three catalytic sites, which are predominantly within the $\beta$ subunits, are in different conformations, depending on the specific interactions with the $\gamma$ subunit. The X-ray crystal structure of bovine $F_1$ (*8*) shows that two of the catalytic sites are in closed conformations with the bound nucleotides confined in a cleft inaccessible to solvent, and the third site is open to solvent. In addition, there are three noncatalytic nucleotide sites predominantly in the $\alpha$ subunits. During ATP hydrolysis, the catalytic reaction forces the rotation of the $\gamma$ subunit and the rotation invokes conformational changes in all three catalytic sites. Generally, chemical cross-links between rotor and stator subunits (*9*−*12*) or between stator subunits (*13*, *14*) impede rotation and catalysis. Perturbation of some specific interactions between the rotor $\gamma$ subunit and the stator $\beta$ subunits cause inefficient coupling between catalysis and rotation, which indicate the critical role of the rotor in coordinating the catalytic mechanism (*15*−*17*). Furthermore, interactions among the sites that are mediated in part through the $\alpha$ subunits are also important in defining the conformation of each site and the interactions with substrates and products. Several mutations in the $\alpha$ subunit have been characterized that block the transmission of information between sites (*18*−*22*).

Despite the considerable information from high-resolution structures and other types of analyses, coordination of the catalytic mechanism and rotation is not well understood. The rotational mechanism carries out energy coupling between the chemistry of ATP hydrolysis or synthesis and the mechanical and conformational coupling to direct $H^+$ transport across the membrane through the $F_O$ sector of the complex. Several lines of evidence indicate that catalysis of ATP hydrolysis that is efficiently coupled to $\gamma$ subunit rotation only occurs during steady-state turnover when all three catalytic sites are involved. Even though two of the catalytic sites bind ATP with high affinity ($<1 \times 10^{-8}$ and $8 \times 10^{-7}$ M), Weber et al. (*23*) demonstrated that rate enhancement of ATP hydrolysis coincides with the occupancy of the third catalytic site, which has a $K_d$ for Mg·ATP of $2-5 \times 10^{-5}$ M. The very similar values for the steady state $K_M$ for Mg·ATP hydrolysis and the $K_M$ for activating rotation of the $\gamma$ subunit (*24*) indicate that rotation is an integral part of the three site catalytic mechanism. In contrast, at very low [Mg·ATP] where the substrate is sub-stoichiometric, ATP binds only in the first high affinity site and is hydrolyzed with slow kinetics (*25*−*28*).

† This work was supported by PHS grant R01-GM50957.

* To whom correspondence should be addressed: Tel: 434-982-0279. Fax: 434-982-1616. E-mail: rkn3c@virginia.edu.

‡ Current address: The Institute of Environment and Resources, 142 To Hien Thanh, 10 Dist., HoChiMinh City, Vietnam.

10.1021/bi700610m CCC: $37.00 
Published on Web 07/10/2007

Significantly, such uni-site catalysis is not associated with rotation (*29*).

To gain a mechanistic understanding of the coupling between catalysis and rotation, we have dissected the elementary rate constants of experimentally accessible reactions leading up to the rate-limiting step and the onset of steady-state hydrolysis. We fit and simulated the pre-steady-state and steady-state kinetics for a wide range of substrate concentrations using a minimal kinetic model. Through these studies, we find that the pre-steady-state kinetics of ATP hydrolysis upon rapid filling of all three catalytic sites indicates that ATP undergoes reversible hydrolysis and synthesis with ADP and Pi at one site and that a rate-limiting conformation change occurs kinetically before the release of Pi. The results fit uniquely to a rotational catalytic scheme involving all three catalytic sites in the following order: (1) Mg·ATP binds to the low affinity site ($\beta_E$, (*8*)); (2) nucleotide bound at the high affinity site ($\beta_{TP}$) undergoes reversible hydrolysis/synthesis;, (3) a rate-limiting step occurs, which likely involves the partial rotation of the $\gamma$ subunit that drives changes of the catalytic sites into the next conformational states; and (4) products Pi and ADP generated in the previous cycle are released from the site, switching from the intermediate affinity ($\beta_{DP}$) site to the low affinity open site ($\beta_E$).

## EXPERIMENTAL PROCEDURES

*Enzyme Preparations.* The *E. coli* $F_1$ complex was purified as previously described (*30*) from the *unc* operon deleted strain DK8 (*31*) harboring the high copy number plasmid pBWU13 (*32*). $F_1$ preparations were replete with $\delta$ and $\epsilon$ subunits as verified by SDS−PAGE analysis and the expected $k_{cat}$ for steady-state ATP hydrolysis rates as reported by Al-Shawi and Senior (*30*). The $\beta$Y331W mutant was expressed from the same plasmid except for the introduction of the tryptophan codon (from TAC to TGG) as previously described (*22*). The $\epsilon$ subunit was expressed with an amino terminal polyhistidine tag (His-$\epsilon$) in the strain BL21(DE3)-*pLysS* as described by Andrews et al. (*33*). His-$\epsilon$ was purified in a manner similar to that previously described (*33*) except that the cell lysate was applied to a Ni-NTA resin column (Qiagen Inc., Valencia, CA) and washed initially using buffer with no imidazole and then using an imidazole gradient of 0−40 mM over four column volumes. Elution of His-$\epsilon$ was achieved using another gradient (40−250 mM imidazole) over four additional column volumes. Incubation with rTEV protease (Life Technologies, Gaithersburg, MD) cleaved the polyhistidine tag. The free His-tags, the His-tagged rTEV protease, and uncleaved $\epsilon$ subunit were separated from purified $\epsilon$ by passage over a Talon affinity column (Clontech, Palo Alto, CA). A greater yield of $\epsilon$ is achieved with the use of Talon resin at this stage rather than Ni-NTA resin because there is less nonspecific binding of cleaved $\epsilon$ to the Talon column.

The $F_1$ enzyme was prepared for kinetic experiments by dilution to ~2 mg/mL in 25 mM TES[1]-KOH, 0.244 mM $MgSO_4$, and 0.2 mM EDTA at pH 7.5 at 25 °C, and passage through two Sephadex G50 centrifuge columns (*34*) equilibrated with the same buffer. The protein concentration was determined by the method of Lowry et al. (*35*). Passing the multisubunit enzyme over centrifuge columns results in the loss of a small portion of the $\epsilon$ subunit from $F_1$. To compensate, 2−3 $\mu$M (approximately one-half the molar concentration of $F_1$) $\epsilon$ was added to $F_1$ after each passage over the centrifuge columns. $F_1$ was then diluted to 1 $\mu$M in the same buffer as described above and used within 2 h.

*Determination of Bound Nucleotid*e. A known amount of $F_1$ enzyme was precipitated by the addition of 0.12 M perchloric acid and allowed to incubate on ice for 10 min. The protein was subsequently removed by centrifugation and the supernatant neutralized by the addition of Trizma base (Sigma-Aldrich) to a final concentration of 107 mM. An aliquot of the sample was subjected to ion exchange HPLC using a Titansphere $TiO_2$ column (Alltech Assoc., Deerfield, IL). The chromatographic assay was performed in a manner similar to that used by Kimura et al. (*36*) using a mobile phase composed of 50 mM $NaH_2PO_4$ buffer at pH 8.0 in 50% v/v acetonitrile with a flow rate of 1 mL/min at 40 °C. The ADP and ATP-associated absorbance at 259 nm was integrated and the amount of nucleotide determined against standard amounts of ADP or ATP chromatographed over the same matrix.

*Pre-Steady-State Hydrolysis of [$\gamma$-$^{32}$P]ATP*. The millisecond time courses of [$\gamma$-$^{32}$P]ATP hydrolysis were generated using a Kintek (Austin, TX) RQF-3 rapid quench-flow apparatus with circulating water temperature control. Mixing and quenching times were verified by carrying out the following calibration reactions: (1) for times less than 40 ms, hydrolysis of benzylidenemalononitrile by NaOH at 20 °C was followed according to the Kintek instruction manual. We observed a $k_{app}$ of 147 $s^{-1}$ for the first-order reaction, which was quite close to the expected 140 $s^{-1}$. (2) For times longer than 25 ms, we followed the hydrolysis of 2,4-dinitrophenylacetate by NaOH to produce 2,4-dinitrophenol and acetate at 25 °C. This was necessary to avoid instrument artifacts that frequently appear in the intermediate times (Scanlon, J. A. B., Al-Shawi, M. K., and Nakamoto, R. K., unpublished data). We found that a thorough calibration of the instrument required that these reactions cover all time phases. Therefore, different concentrations of NaOH were used to give the appropriate rate for the desired time range. A second-order rate constant of 57.6 $M^{-1}$ $s^{-1}$ was obtained for this reaction, which was in good agreement with previously published values (*37*).

The components of each syringe in the rapid mixing device (1:1 mixing volume ratio) were as follows: syringe A contained purified $F_1$ (with an additional equimolar concentration of $\epsilon$ subunit), prepared as described above, and syringe B contained 25 mM TES-KOH, 0.2 mM EDTA at pH 7.5 at 25 °C, and varying concentrations of [$\gamma$-$^{32}$P]ATP and $MgSO_4$. The following Mg·ATP concentrations were obtained with the indicated [$\gamma$-$^{32}$P]ATP and $MgSO_4$ concentrations after mixing in the chemical quench instrument: 260 $\mu$M Mg·ATP final, 1.266 mM [$\gamma$-$^{32}$P]ATP, and 0.764 mM $MgSO_4$; 106 $\mu$M Mg·ATP final, 1 mM [$\gamma$-$^{32}$P]ATP, and 0.46 mM $MgSO_4$; 62 $\mu$M Mg·ATP final, 0.245 mM [$\gamma$-$^{32}$P]ATP, and 0.33 mM $MgSO_4$; 29.2 $\mu$M Mg·ATP final, 0.267 mM [$\gamma$-$^{32}$P]-ATP, and 0.23 mM $MgSO_4$; 17.8 $\mu$M Mg·ATP, 0.087 mM [$\gamma$-$^{32}$P]ATP, and 0.278 mM $MgSO_4$; and 4.8 $\mu$M Mg·ATP, 0.011 mM [$\gamma$-$^{32}$P]ATP, and 0.252 mM $MgSO_4$. Reactions, which were run at 25 °C, were quenched by the rapid

[1] Abbreviations: TES, 2-[(2-hydroxy-1,1-bis(hydroxymethyl)ethyl)-amino]ethanesulfonic acid; MSC, model selection criterion.

Scheme 1


addition of 1 mM $KH_2PO_4$ in 0.033 N perchloric acid (final concentration). A two step procedure was developed to minimize problems with the high background due to the high concentration of [$\gamma$-$^{32}$P]ATP used in these experiments. First, an equal volume of 1% (w/v) ice-cold acid-activated charcoal suspension (Norit, Sigma Chemicals, St. Louis, MO) was added to the quenched sample and incubated on ice for 10 min. The charcoal was removed by centrifugation at 22,000*g* for 10 min, and 400 $\mu$L of the cleared supernatant was centrifuged at 426,000*g* for a further 7 min to remove any finer particles. This treatment removed 96% of the unreacted ATP. Then, 300 $\mu$L of the final supernatant was diluted with 300 $\mu$L of 0.6 N perchloric acid plus 1 mM $KH_2PO_4$. The second step was the precipitation of inorganic phosphate by the addition of 600 $\mu$L of acid molybdate solution (*38*). After incubating on ice for 20 min, the precipitate was centrifuged at 22,000*g* and the supernatant removed. The pellet was washed once with 1 mL of 0.16 N perchloric acid. The final pellet was dissolved by the addition of 1 M NaOH and the radioactivity determined by Cherenkov counting in 15 mL of 0.2 M Trizma base. Background samples were prepared by adding quench solution to the protein before the addition of substrate and radioactivity. These samples were processed in the same manner and subtracted from the time point samples.

*Determination of Kinetic Constants for ATP Hydrolysis.* Steady-state ATP hydrolysis was measured in essentially the same conditions as those of the pre-steady-state experiments described above, using [$\gamma$-$^{32}$P]ATP and measuring Pi production. All buffers were designed so that the concentration of free $Mg^{2+}$ was constant at approximately 50 $\mu$M. A bent-tipped syringe was used for rapid mixing of 15 $\mu$L of substrate (*39*) with an equal volume of 1 $\mu$M $F_1$ in a vortexed tube. The reaction was quenched at various time points with 1 mM $KH_2PO_4$ in 0.03 N perchloric acid (final concentrations). Samples were processed following the same two step protocol developed for samples in the pre-steady-state experiments for the removal of excess background [$\gamma$-$^{32}$P]-ATP. Zero time points were acquired by mixing quench solution and protein before the addition of substrate. The reaction medium for the determination of kinetic constants as a function of Mg·ATP contained 25 mM TES, 0.2 mM EDTA, and varying concentrations of ATP (0−1.26 mM ATP) and $MgSO_4$ (0.245−0.764 mM) to ensure a final low free $Mg^{2+}$ concentration of approximately 50 $\mu$M at pH 7.5 at 25 °C. ATP hydrolysis rates were determined from time points measured from 1−10 s.

The inhibitory constant of ADP ($K_I^{ADP}$) was determined in buffer where Mg·ATP was held constant at 105 $\mu$M, and ADP was increased from 0 to 1 mM. The buffer contained 25 mM TES, 0.2 mM EDTA, 0.35 mM $MgSO_4$, and 0.25 mM ATP, and to keep the free $Mg^{2+}$ constant, additional $MgSO_4$ was supplemented with ADP in a constant molar ratio. ATP hydrolysis rates were determined for a time course in each reaction condition of 1−10 s.

*Pre-Steady-State Nucleotide Binding*. Nucleotide binding to the catalytic sites was monitored by the decrease in tryptophan fluorescence intensity of the $\beta$Y331W mutant $F_1$ as previously described (*23*). The kinetics of fluorescence quenching were followed in an Applied Photophysics SX.18MV-R stopped-flow spectrometer (Surrey, U.K.). The excitation wavelength was 295 nm, and emission was monitored through a 320 nm cutoff filter in the stopped-flow apparatus (or at 360 nm in the steady-state fluorimeter). The syringe contents were essentially the same as those for the rapid quench flow experiments except for the lack of radioactivity. The conditions for the Mg·ATP titration were as follows: syringe A contained 1 $\mu$M purified $F_1$, prepared as described above, and syringe B contained 25 mM TES-KOH, 0.2 mM EDTA at pH 7.5 at 25 °C, and ATP and $MgSO_4$ concentrations that resulted in a final free $Mg^{2+}$ concentration of 50 $\mu$M and the following Mg·ATP concentrations: 519 $\mu$M Mg·ATP, 1.26 mM ATP, and 0.764 mM $MgSO_4$; 260 $\mu$M Mg·ATP, 0.63 mM ATP, and 0.504 mM $MgSO_4$; 104 $\mu$M Mg·ATP, 0.252 mM ATP, and 0.348 mM $MgSO_4$; 40 $\mu$M Mg·ATP, 0.097 mM ATP, and 0.284 mM $MgSO_4$; 17.3 $\mu$M Mg·ATP, 0.042 mM ATP, and 0.261 mM $MgSO_4$; 10.4 $\mu$M Mg·ATP, 0.025 mM ATP, and 0.254 mM $MgSO_4$; 4 $\mu$M Mg·ATP, 0.0097 mM ATP, and 0.248 mM $MgSO_4$; and 1 $\mu$M Mg·ATP, 0.0025 mM ATP, and 0.245 mM $MgSO_4$. The ADP titration conditions were the same for syringe A, and syringe B contained 25 mM TES-KOH, 0.2 mM EDTA at pH 7.5 at 25 °C, and varying concentrations of ADP and $MgSO_4$. The following combinations resulted in the indicated ADP concentration and a final free $Mg^{2+}$ of 50 $\mu$M: 2000 $\mu$M ADP and 0.326 mM $MgSO_4$; 1000 $\mu$M ADP and 0.285 mM $MgSO_4$; 500 $\mu$M ADP and 0.264 mM $MgSO_4$; 250 $\mu$M ADP and 0.254 mM $MgSO_4$; 250 $\mu$M ADP and 0.254 mM $MgSO_4$; 100 $\mu$M ADP and 0.248 mM $MgSO_4$; 50 $\mu$M ADP and

Table 1: Rate Constants Derived from Kinetic Fits[a]

| [Mg·ATP] $\mu$M | $k_{+1}$ $M^{-1}$ $s^{-1}$ $\times10^7$ | $k_{-1}$ $s^{-1}$ $\times10^4$ | $K_1$ $M^{-1}$ $\times10^3$ | $K_d^{ATP}$ $\mu$M | $k_{+2}$ $s^{-1}$ | $k_{-2}$ $s^{-1}$ | $K_2$ | $k_\gamma$ $s^{-1}$ | $k_{+3}$ $s^{-1}$ | $k_{-3}$ $M^{-1}$ $s^{-1}$ | $K_3$ $M^{-1}$ $\times10^{-2}$ | $K_d^{Pi}$ M | $k_{+4}$ $s^{-1}$ | $k_{-4}$ $M^{-1}$ $s^{-1}$ $\times10^6$ | $K_4$ $M^{-1}$ $\times10^4$ | $K_d^{ADP}$ $\mu$M | $R^2$ | MSC[b] |
|---|---|---|---|---|---|---|---|---|---|---|---|---|---|---|---|---|---|---|
| 4.8 | 4.0 | 2.0 | 2.0 | 50 | 94 | 95 | 1.0 | 24 | 200 | 8.9 | 4.4 | 22 | 250 | 3.0 | 1.2 | 83 | 0.997 | 4.92 |
| 17.8 | 3.0 | 1.6 | 1.9 | 53 | 100 | 98 | 1.0 | 29 | 210 | 12 | 5.8 | 17 | 380 | 4.0 | 1.0 | 95 | 0.997 | 5.08 |
| 29.2 | 4.5 | 1.8 | 2.5 | 40 | 140 | 140 | 1.0 | 30 | 210 | 12 | 5.8 | 17 | 380 | 4.5 | 1.2 | 85 | 0.997 | 5.08 |
| 62.0 | 4.2 | 2.1 | 2.0 | 50 | 140 | 140 | 1.0 | 30 | 210 | 14 | 6.7 | 15 | 380 | 4.5 | 1.2 | 85 | 0.998 | 5.56 |
| 105.6 | 4.2 | 2.1 | 2.0 | 50 | 170 | 110 | 1.5 | 29 | 210 | 14 | 6.7 | 15 | 380 | 4.5 | 1.2 | 85 | 0.998 | 5.56 |
| 259.9 | 4.0 | 2.1 | 1.9 | 53 | 170 | 110 | 1.5 | 30 | 200 | 13 | 6.6 | 15 | 380 | 4.5 | 1.2 | 85 | 0.994 | 4.40 |
| average | 4.0 | 1.9 | 2.0 | 49 | 140 | 120 | 1.2 | 29 | 210 | 12 | 6.0 | 17 | 360 | 4.2 | 1.2 | 86 | | |
| ±SE | ± 0.2 | ± 0.1 | ± 0.1 | ± 2 | ± 13 | ± 8 | ± 0.1 | ± 0.9 | ± 2 | ± .0.8 | ± 0.4 | ± 1.1 | ± 22 | ± 0.2 | ± 0.0 | ± 2 | | |

[a] Rate constants refer to Scheme 1. [b] See Experimental Procedures for the definition of MSC, the model selection criterion.

Table 2: Sensitivity Analysis of Kinetic Constants: Model Selection Criterion (MSC) Values for Fits Using Alternative Kinetic Constants[a]

| best fit MSC: 5.56 | $k_{+1}$ | $k_{-1}$ | $k_{+2}$ | $k_{-2}$ | $k_{+2}$: $k_{-2}$[b] | $k_{\gamma}$ | $k_{+3}$ | $k_{-3}$ | $k_{+4}$ | $k_{-4}$ |
|---|---|---|---|---|---|---|---|---|---|---|
| 10-fold ↑ | N.F.[d] | N.F. | N.F. | N.F. | 2.96[c] | N.F. | 4.45 | 5.30 | 4.56 | 3.87 |
| 10-fold ↓ | N.F. | N.F. | N.F. | N.F. | 1.30 | N.F. | 3.12 | 5.30 | 2.38 | 5.09 |
| 2-fold ↑ | 2.35 | 2.31 | N.F. | 1.46 | 3.93 | N.F. | 4.85 | 5.30 | 5.39 | 5.39 |
| 2-fold ↓ | 2.29 | 2.37 | 1.13 | 1.18 | 3.76 | 1.08 | 5.44 | 5.44 | 5.38 | 5.20 |

[a] The 62 $\mu$M [Mg·ATP] data set was used for the sensitivity analysis of the rate constants. Details of the procedure are described further in Experimental Procedures. [b] Both parameters are increased/decreased simultaneously, thus retaining the ratio of the parameter, $K_2$. [c] The MSC (*42*), which is defined in Experimental Procedures, is a highly sensitive parameter for distinguishing between models and selects the best model that fits with simplicity and parsimony. The MSC is a relative value and should be compared to the best fit MSC of 5.56 for this data set (the higher the MSC value, the more appropriate the model). [d] NF: no fit because of undefined parameters, negative MSC values, or rate constants that were unrealistic.

0.246 mM $MgSO_4$; 20 $\mu$M ADP and 0.245 mM $MgSO_4$; 10 $\mu$M ADP and 0.2444 mM $MgSO_4$; and 5 $\mu$M ADP and 0.2442 mM $MgSO_4$. The kinetic fluorescence curves shown in Figure 4 were generated from 2 to 4 stopped-flow mixing experiments. Nucleotide occupancy was determined on the basis of the affinity constants for $\beta$Y331W as described by the Senior laboratory (*23*).

*Model Fitting and Sensitivity Analysis.* Differential equation integration, location of the region of the minimum, fitting of experimental data, model simulations, and statistical analyses were performed using the experimental data fitting program Scientist, version 2.0 (Micromath Research, Inc., St Louis, Missouri). The Scientist program solves systems of model equations, generates fits to the data, and simulates all other parameters, yielding progress curves for all species. Differential equations for the whole reaction scheme (Scheme 1) were set up as follows:

$$d[F_1]/dt = -k_{+1}[F_1][ATP] + k_{-1}[F_1{\cdot}ATP] + k_{+4}[F_1''{\cdot}ADP] - k_{-4}[F_1][ADP]$$

$$d[ATP]/dt = -k_{+1}[F_1][ATP] + k_{-1}[F_1{\cdot}ATP]$$

$$d[F_1{\cdot}ATP]/dt = k_{+1}[F_1][ATP] - k_{-1}[F_1{\cdot}ATP] - k_{+2}[F_1{\cdot}ATP] + k_{-2}[F_1{\cdot}ADP{\cdot}Pi]$$

$$d[F_1{\cdot}ADP{\cdot}Pi]/dt = k_{+2}[F_1{\cdot}ATP] - k_{-2}[F_1{\cdot}ADP{\cdot}Pi]$$

$$d[F_1''{\cdot}ADP{\cdot}Pi]/dt = k_{\gamma}[F_1{\cdot}ADP{\cdot}Pi] - k_{+3}[F_1''{\cdot}ADP{\cdot}Pi] + k_{-3}[F_1''{\cdot}ADP][Pi]$$

$$d[F_1''{\cdot}ADP]/dt = k_{+3}[F_1''{\cdot}ADP{\cdot}Pi] - k_{-3}[F_1''{\cdot}ADP][Pi] - k_{+4}[F_1''{\cdot}ADP] + k_{-4}[F_1][ADP]$$

$$d[Pi]/dt = k_{+3}[F_1''{\cdot}ADP{\cdot}Pi] - k_{-3}[F_1''{\cdot}ADP][Pi]$$

$$d[ADP]/dt = k_{+4}[F_1''{\cdot}ADP] - k_{-4}[F_1][ADP]$$

$$Q = [F_1{\cdot}ADP{\cdot}Pi] + [F_1''{\cdot}ADP{\cdot}Pi] + [Pi]$$

where $Q$ represents the quench-flow data, that is, the amount of Pi generated. $F_1$ and $F_1''$ represent the enzyme in different conformational states, which is necessary to distinguish the concentrations of $F_1{\cdot}ADP{\cdot}Pi$, the state before the putative $\gamma$ subunit rotation step, $k_{\gamma}$, and $F_1''{\cdot}ADP{\cdot}Pi$, the state after $k_{\gamma}$. The numerical integration of the differential equations was performed using the EPISODE integrator package for stiff systems (where there are large differences in the way two or more dependent variables depend on the independent variable, e.g., kinetic rate constants with large differences in rates). The analytic Jacobian matrix was used internally in the EPISODE integrator so that at each step of the corrector iteration it solves systems of nonlinear equations that arise. Parameters were initially estimated on the basis of the experimental evidence described in this article and from previously published work. These initial parameters were refined using the simplex technique (*40*) in Scientist v2.0, which searches the parameter space to locate the region of the local minima. A nonlinear least-squares fit was then performed using the refined parameters. The least-squares minimization in Scientist v2.0 is based on the algorithm by Powell (*41*), but it is altered to automatically include the scaling of variables and also systems with more unknowns than equations. The two steps, simplex searching to improve parameter estimates followed by least-squares minimization, were performed until the best fits were determined for each [Mg·ATP] condition.

The goodness-of-fit of the simulations to the data were determined partly by the $R^2$ parameter, but the more sensitive parameter used for most evaluations was the model selection criterion (MSC; see ref *42*). The MSC is a modified Akaike information criterion (AIC) (*43*, *44*). The AIC is a statistical method that objectively distinguishes between different models, selecting the model that fits well but with the fewest parameters, i.e., it selects for simplicity and parsimony. In this way, it attempts to represent the information content of a set of parameter estimates (relating the fraction of variability to the number of parameters used to obtain the fit). The AIC and MSC give the same rankings between models, but the AIC is dependent on the number of observations and the magnitude of the data points. The MSC is a reciprocal form of the AIC and has been normalized so that it is independent of the scaling of the data points (*42*). Essentially, the larger the MSC value, the more appropriate the model.

A sensitivity analysis of each parameter was performed. The data set for 62 $\mu$M Mg·ATP was used for the analysis because it gave an excellent fit to our model (MSC: 5.56). The partial rate constants represented those of the other conditions very well, and it was the highest [Mg·ATP] concentration with minimal scatter of the data points. The parameters for the best fit to this data set are listed in Table 1 and were used for the sensitivity analysis. Each rate constant was perturbed individually (10-fold or 2-fold) as listed in Table 2, while the other rate constants were not varied. These parameter sets were used as seed values for a minima-seeking simplex algorithm, which improved initial

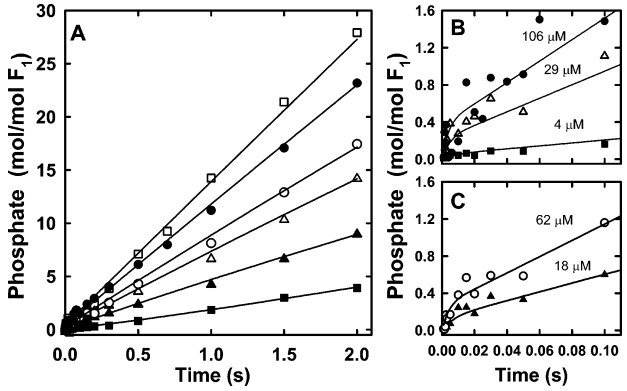


FIGURE 1: Pre-steady-state hydrolysis by $F_1$ after fast addition of various concentrations of Mg·ATP. (A) The complete time course up to 2.0 s. Purified $F_1$ was prepared for each Mg·ATP condition as described in Experimental Procedures and diluted to 1 $\mu$M in 25 mM TES-KOH, 0.244 mM $MgSO_4$, and 0.2 mM EDTA at pH 7.5 at 25 °C and loaded into syringe A of the chemical quench instrument. The [$\gamma$-$^{32}$P]ATP and $MgSO_4$ concentrations in syringe B resulted in the following final [Mg·ATP]: 260 $\mu$M Mg·ATP (□);106 $\mu$M Mg·ATP (●); 62 $\mu$M Mg·ATP (○); 29.2 $\mu$M Mg·ATP (△); 17.8 $\mu$M Mg·ATP (▲); and 4.8 $\mu$M Mg·ATP (■). The lines show the best fit to each condition based on Reaction Scheme 1 and the constants in Table 1. (B) The early time points up to 0.1 s for 106 $\mu$M Mg·ATP (●), 29.2 $\mu$M Mg·ATP (△), and 4.8 $\mu$M Mg·ATP (■). (C) The early time points up to 0.1 s for 62 $\mu$M Mg·ATP (○) and 17.8 $\mu$M Mg·ATP (▲). The early time course for the 260 $\mu$M Mg·ATP data set is omitted for clarity.

parameter estimates for the subsequent nonlinear least-squares analysis that fit the parameter set to the experimental data. The simplex search and least-squares analysis could not be completed for the most sensitive parameters because of undefined numbers. In cases where the model fit was performed successfully, the deviations of the model curves from the data were assessed visually and by performing a statistical analysis to determine the MSC values of the fits.

*Other Procedures*. Except where [$\gamma$-$^{32}$P]ATP was used, steady-state ATPase activities were determined colorimetrically as previously described (*15*). Concentrations of free $Mg^{2+}$, free ATP, Mg·ATP, and Mg·ADP were calculated using the algorithm of Fabiato and Fabiato (*45*). All chemicals and reagents were of the highest quality available.

## RESULTS

*Design of Experimental Conditions for Pre-Steady-State ATP Hydrolysis by $F_1$*. As discussed in the Introduction, experimental results from several laboratories contribute to the hypothesis that ATP hydrolysis is coupled to $\gamma$ subunit rotation only at ATP concentrations high enough to occupy all three catalytic sites. Consequently, the determination of pre-steady-state kinetics of the rotational catalytic pathway must be initiated with Mg·ATP concentrations similar to the $K_M$ for steady-state ATPase activity, that is, in the range of $10^{-5}-10^{-4}$ M. The true substrate of $F_1$ is Mg·ATP, and excess free $Mg^{2+}$ is well known to be inhibitory (*46*). Conditions were therefore chosen with an excess of ATP over total $Mg^{2+}$, with free $Mg^{2+}$ buffered at 50 $\mu$M. Furthermore, it was necessary to use radioactive [$\gamma$-$^{32}$P]ATP because we needed to be able to detect stoichiometric amounts of Pi in the first few turnovers of the enzyme. Reaction conditions used for the time course of ATP hydrolysis given in the legend to Figure 1 and Experimental Procedures are a compromise to satisfy these requirements and to ensure that the enzyme is working in a multisite catalytic mode maximally coupled to rotation.

The large background due to [$\gamma$-$^{32}$P]ATP levels compared to the small amounts of Pi produced and the nonenzymatic hydrolysis of [$\gamma$-$^{32}$P]ATP during downstream sample processing were reduced by developing a protocol for quantitative separation of Pi produced from the total background ATP. A two-step procedure was used to remove ATP from the acid quenched solution (see Experimental Procedures): first, treatment with acid-activated charcoal and its subsequent removal by centrifugation and second, precipitation of Pi with acidic molybdate solution (*38*). This allowed the effective separation of Pi produced from background ATP, which was typically 100−1000-fold in excess.

Another consideration is the nucleotide occupancy of the enzyme at the beginning of the reaction. ADP bound to all three catalytic sites may slow the onset of catalysis (*47*), whereas an enzyme completely devoid of nucleotide may behave differently because the noncatalytic sites will need to refill before the complex reacquires the normal steady-state load of nucleotide. Purified $F_1$ was gently treated by passage through two centrifuge columns as described in the Experimental Procedures to remove the nucleotide from two catalytic sites while leaving nucleotides in the noncatalytic sites. An ion exchange HPLC assay (see Experimental Procedures) was used to determine whether the starting enzyme contained 4.1 ± 0.1 bound nucleotides per $F_1$, of which 2.9 ± 0.1 mol were ATP and 1.1 ± 0.03 mol were ADP (from three independent determinations). On the basis of previous determinations, we assumed that three ATP are in noncatalytic sites and one ADP is in a catalytic site (*48*, *49*).

*Pre-Steady-State Measurement of ATP Hydrolysis at High [Mg·ATP]*. The pre-steady-state kinetics of ATP hydrolysis was analyzed to determine the rate constants of the partial reactions of the enzyme in catalytic mode involving the rotation of the $\gamma$ subunit. The data sets and fits (Figure 1, Table 1, and discussed in detail below) show the activation of steady-state ATP hydrolysis rates for a range of Mg·ATP concentrations from 4.8 to 260 $\mu$M. These data sets are representative of several experiments repeated at all Mg·ATP concentrations and with several different enzyme preparations. As can be clearly seen in the faster time frame (Figure 1B and C, separated into two frames for clarity), ATP hydrolysis occurs with an initial burst within the first 10−20 ms and then enters into the slower steady-state phase. (The enzyme enters the steady-state mode at ~50 ms under all conditions.) The scatter in the data at the early time points of the higher concentrations (Figure 1B and C) was unavoidable because of the high background. Despite this limitation, the higher quality data for the lower concentrations and for the longer time points of the higher concentrations, allow us to obtain confident fits including the initial burst of hydrolysis of Mg·ATP.

The number of sites involved in the burst was determined using the individual fits for each condition, back extrapolating the steady-state rates (from 50 ms onward) to zero time and fitting these values to the Michaelis−Menten equation to give an active site titration (Figure 2). This analysis gave a stoichiometry of 0.5, indicating that one active site per $F_1$ molecule gives rise to the burst and additionally that the ATP

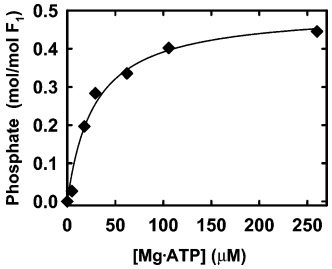


FIGURE 2: Analysis of the burst of hydrolysis. The active site titration described in Results was a back extrapolation to zero time of the steady-state rates for the individual fits to the pre-steady-state data in Figure 1. The solid line shows the fit to the data using the Michaelis−Menten equation and gives a stoichiometry of 0.5 sites per $F_1$ molecule.

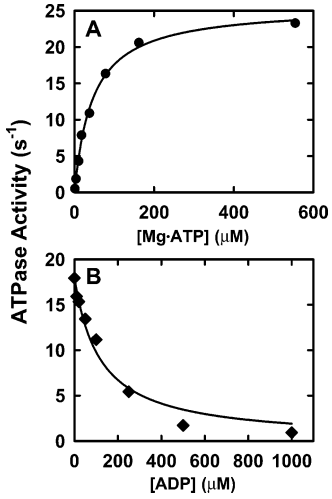


FIGURE 3: Titrations to determine the steady-state kinetic constants of Mg·ATP hydrolysis. $F_1$ was prepared in the same way as the pre-steady-state experiments described in Experimental Procedures. Initial steady-state rates of hydrolysis of Mg·ATP were measured over a range of concentrations using [$\gamma$-$^{32}$P]ATP and measuring Pi production. All buffers contained 25 mM TES-KOH, 0.2 mM EDTA, and 0.244 mM $MgSO_4$ at pH 7.5 at 25 °C. ATP, ADP, and Pi were added in increasing concentrations with additional $MgSO_4$ to ensure a final free [$Mg^{2+}$] of approximately 50 $\mu$M for all conditions. The lines drawn are fits to the data using the Michaelis−Menten equation. (A) (●) ATP hydrolysis rates for varying concentrations of Mg·ATP (1−519 $\mu$M). Parameters for the fit: apparent $K_M$ for ATP = 44.8 $\mu$M and $V_{max}$ = 25.6 $s^{-1}$. (B) ATP hydrolysis rates measured with increasing concentrations of ADP (♦). The [Mg·ATP] was held constant at 105 $\mu$M, ADP was increased from 0 to 1 mM, and $MgSO_4$ was supplemented with ADP at a constant molar ratio. Parameters for the fit: $K_I$ for ADP = 119 $\mu$M and $k_{cat}$ = 18 $s^{-1}$.

and ADP + Pi bound to the enzyme are carrying out reversible hydrolysis/synthesis. An apparent $K_M$ of 51 $\mu$M was calculated from the steady-state rates in the quench flow instrument, which was essentially the same as the apparent $K_M$ of 45 $\mu$M for the steady-state hydrolysis of Mg·ATP determined in hand-mixing measurements under the same conditions (Figure 3A) and by Weber et al. using $\beta$Y331W $F_1$ (*23*, *50*). These $K_M$ values also match the $K_d$ for the third low affinity site measured in Figure 4A. The agreement of these values strongly suggests that the pre-steady-state burst of hydrolysis is due to the binding of Mg·ATP to the third catalytic site.

*Kinetic Constants Determined for Mg·ATP and ADP under Conditions Used for Pre-Steady-State Experiments.* In order to ensure the veracity of pre-steady-state experiments and

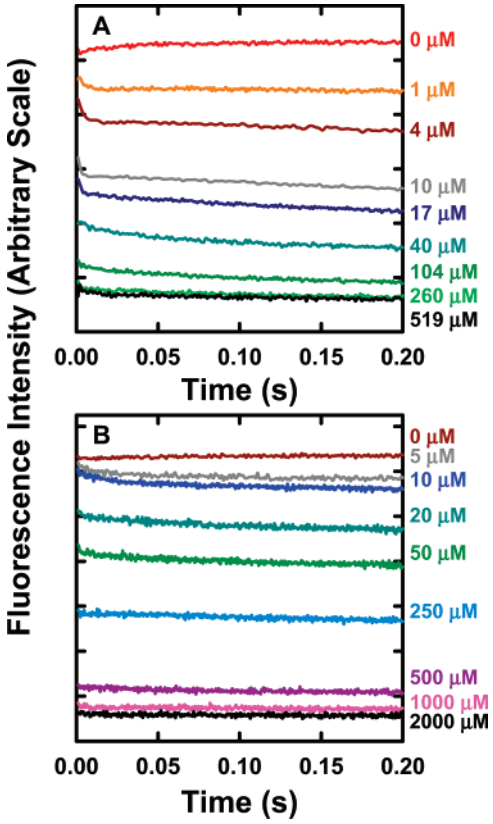


FIGURE 4: Pre-steady state association of Mg·ATP and ADP with the $\beta$Y331W mutant $F_1$. The binding of Mg·ATP or ADP to the $\beta$Y331W mutant $F_1$ was followed by the decrease of tryptophan fluorescence as previously described (*22*, *23*). Details are given in Experimental Procedures for the stopped-flow setup. $F_1$ was prepared as described in the Experimental Procedures and contained 3.8 ± 0.2 mol nucleotide bound per mol $F_1$. Syringe A contained 1 $\mu$M $F_1$ in 25 mM TES-KOH, 0.2 mM EDTA, and 0.244 mM $MgSO_4$ at pH 7.5 at 25 °C. (A) The ATP and $MgSO_4$ concentrations in syringe B resulted in a final free $Mg^{2+}$ of 50 $\mu$M and the following [Mg·ATP]: 519 $\mu$M Mg·ATP; 260 $\mu$M Mg·ATP; 104 $\mu$M Mg·ATP; 40 $\mu$M Mg·ATP; 17.3 $\mu$M Mg·ATP; 10.4 $\mu$M Mg·ATP; 4 $\mu$M Mg·ATP; and 1 $\mu$M Mg·ATP. (B) The ADP and $MgSO_4$ concentrations in syringe B resulted in a final free $Mg^{2+}$ of 49 $\mu$M and the following [ADP]: 2000 $\mu$M ADP; 1000 $\mu$M ADP; 250 $\mu$M ADP; 100 $\mu$M ADP; 20 $\mu$M ADP; 10 $\mu$M ADP; and 5 $\mu$M ADP.

to validate model fits to the pre-steady-state rapid kinetic data, it was important to determine the steady-state kinetic constants of Mg·ATP hydrolysis and ADP inhibition under the same conditions. The $K_M$ and $V_{max}$ for Mg·ATP steady-state hydrolysis were determined from the fit to the data in Figure 3A. In Figure 3B, the $K_I$ for ADP was determined by measuring the initial rates of Mg·ATP hydrolysis ([Mg·ATP] = 105 $\mu$M) under conditions with increasing concentrations of ADP. The $K_I$ for ADP was determined from the data fit to be 119 $\mu$M, which is in good agreement with the $K_d$ value determined from experiments of ADP binding to the $\beta$Y331W mutant discussed later. The values of steady-state kinetic constants measured under the conditions stated here are similar to published values and the steady-state parameters determined in the rapid quench flow experiments.

*Pre-Steady-State Binding of Mg·ATP and Mg·ADP Monitored by Fluorescence Quenching of the $\beta$Y331W Mutant.* In order to establish that binding of Mg·ATP to the three catalytic sites occurs with compatible kinetics to the rapid burst of Mg·ATP hydrolysis, the fluorescence quenching of

the $\beta$Y331W mutant $F_1$ (*23*) was followed in the stopped-flow spectrometer. The experiments in Figure 4 were performed under the same conditions as those of the quench flow experiments, and the $\beta$Y331W mutant $F_1$ was prepared in the same way as wild-type $F_1$, as described in Experimental Procedures. Again, the nucleotide occupancy of the enzyme at the beginning of the reaction was important to determine and was measured by the ion exchange HPLC assay to be 3.8 ± 0.2 mol nucleotide bound per mol $F_1$ (similar to that of the wild-type enzyme).

The rate of binding of Mg·ATP to $F_1$ under the conditions used for the quench-flow experiments is very rapid, as can be seen from Figure 4A. The fluorescence stopped-flow traces were used to calculate nucleotide occupancy as previously described by Weber et al. (*23*). Second-order fits of the data indicate that binding to all three catalytic sites is diffusion-limited ($\sim 1 \times 10^9$ $M^{-1}$ $s^{-1}$). Clearly, the binding of Mg·ATP is not rate limiting to the rest of the reaction. Using the extent of sites filled at 5 ms, the $K_{1/2}$ for rapid binding of Mg·ATP to all three sites was approximately 13 $\mu$M in the same low free $Mg^{2+}$ conditions used in the quench-flow experiments described above. The addition of higher $Mg^{2+}$ (up to 0.89 mM free $Mg^{2+}$) did not strongly affect the binding affinity (data not shown). The binding stoichiometry was calculated from the extent of quenching of $\beta$Y331W fluorescence, and we note that for the 104 $\mu$M Mg·ATP concentration 2.6 sites were filled within the 1 ms dead time of the instrument. Binding of Mg·ATP to the first site is known to occur with high affinity (*51*, *52*). A value for $K_{d1}$ of 5 nM was used to fit the Mg·ATP binding titration to a model with three sites of differing affinities, which gives the following values: $K_{d2} = 2.4$ $\mu$M and $K_{d3} = 44.8$ $\mu$M. This agrees with the $K_{d2} = 0.9$ $\mu$M and $K_{d3} = 33$ $\mu$M values that were previously determined (*23*, *53*). These data greatly strengthen our hypothesis that the initial burst of ATP hydrolysis is driven by the binding of the nucleotide to the third, low affinity catalytic site with a $K_d$ for Mg·ATP that is very similar to the $K_M$ for steady-state Mg·ATP hydrolysis ((*50*) and Figure 3A) and the rotation of the $\gamma$ subunit (*24*).

A titration with ADP using the $\beta$Y331W mutant $F_1$, under the same low free $Mg^{2+}$ conditions as those of the quench-flow experiments, was also performed (Figure 4B). Binding of ADP to the enzyme is rapid, and second-order fits of the data show that the rate is slightly slower than diffusion limited (on the order of $1 \times 10^7 - 1 \times 10^8$ $M^{-1}$ $s^{-1}$). Using the extent of sites filled at 5 ms, the $K_{1/2}$ for the rapid binding of ADP to all three sites was approximately 127 $\mu$M under these conditions. These data could be fit to a model assuming a single class of binding site, with a $K_d$ for ADP of 80 $\mu$M. This value is used for the initial starting value for $k_{+4}/k_{-4}$ in modeling (Table 1) and is in very good agreement with the previously reported values of 83 and 100 $\mu$M (*54*, *55*). In addition, it is similar to the $K_I$ value of 120 $\mu$M determined for the inhibition of steady-state hydrolysis due to increasing ADP concentrations (Figure 3B). These results indicate that under the conditions used for our experiments, where ADP and free $Mg^{2+}$ concentrations are low, there is not enough Mg·ADP present to drive the enzyme into a Mg·ADP inhibited form.

*Modeling Data Fits and Simulations of Pre-Steady-State Reactions.* Our kinetic model, as shown in Scheme 1, shows that a single nucleotide binds, undergoes reversible hydrolysis/synthesis, and releases from the enzyme in each cycle. Even though these steps occur in different catalytic sites and to different nucleotides, which is an essential aspect of the rotational catalytic mechanism as will be described in the Discussion section, only single nucleotide binding and release steps in each cycle are necessary for the purposes of simulating the kinetic model. As will be described in detail in the following section, we emphasize that both the pre-steady-state and steady-state data are critical in constraining the possible kinetic steps and their values. Initial estimates of the rate constants for the model were determined as much as possible from the experimental results shown above. Importantly, both pre-steady-state and steady-state phases were fit by a single kinetic model and set of rate constants.

(*i*) The described model is a minimal model with the least number of steps required to achieve a confident fit. The basic steps of ATP binding, hydrolysis, and Pi and ADP release were taken from a scheme used to describe the reaction at a single catalytic site, also known as the uni-site condition (*25*, *27*), although we emphasize that the multisite, steady-state kinetics are different from the uni-site reaction. All of the rate constants used to fit the data in Figure 1 are faster than those determined in uni-site conditions (*25*, *52*, *56*). In addition, a model with only the four uni-site steps was not adequate to simulate the data. An additional slow step (Scheme 1, Step 3) was required to achieve a good fit to the data, the position of which in the order of the reaction was critical and will be discussed later. This minimal model uniquely simulates both the pre-steady-state and steady-state phases of hydrolysis.

(*ii*) The binding of Mg·ATP was very rapid as determined in Figure 4A. The $k_{+1}$ in the model fits is an apparent binding constant and is not quite as fast as the diffusion-limited rate determined from Figure 4A. We hypothesize, and it is shown in our model (discussed below), that this is due to Mg·ATP binding at one site and hydrolysis occurring at another site, requiring transmission of information between the two sites. This cooperativity occurs in a finite time and therefore slows the apparent binding rate of Mg·ATP in the model. The ratio of $k_{-1}/k_{+1}$ was approximated both from the $K_M$ values and the $K_d$ value for Mg·ATP calculated from Figures 1, 3A, and 4A. The close similarity of the $K_M$ value for Mg·ATP hydrolysis and the $K_{d3}$ value indicates that catalysis is triggered by Mg·ATP binding to the third site.

(*iii*) The forward and reverse constants for the step of ATP hydrolysis ($k_{+2}$ and $k_{-2}$) were not constrained in model fitting. The best fits were achieved when the forward and reverse constants were approximately equal. Even when initial seed values were chosen where the two parameters differed, after performing the simplex and least-squares minimization with high stringency, the $k_{+2}/k_{-2}$ ratio tended toward unity. This is in agreement with the model of Boyer and others ((*57*); see ref *2* for a review), indicating that ATP is undergoing reversible hydrolysis/synthesis with ADP and Pi at the site of chemistry. The sensitivity analysis (Table 2, and described below) validates this notion in that the ratio of the forward and reverse reactions is a highly sensitive parameter, and small changes in the ratio greatly decreased the quality of the fit.

(*iv*) As described above, the rate-limiting step (Step 3) was required to account for the observed initial burst of hydrolysis. The seed value for this step was approximated

by the $V_{max}$ (25.6 $s^{-1}$) for Mg·ATP under the same conditions (Figure 3A). This step was not constrained in model fitting, although it tended not to vary greatly. The order of this step in the reaction scheme was also directly tested (see *viii* below for description). This step could only follow hydrolysis (Step 2) and precede Pi release (Step 4). Previously, it has been argued that a partial rotation of the $\gamma$ subunit in ATP hydrolysis is associated with the decrease in affinity for Pi, allowing Pi release, a major energy yielding step in hydrolysis ((*58*); reviewed in ref *2*). The requirement for a slow step in the model, prior to Pi release, further supports this hypothesis. This rate-limiting step is therefore termed $k_\gamma$.

(*v*) One Pi is released per cycle of the enzyme in the steady-state mode of the model. Pi release, $k_{+3}$, is not the rate-limiting step; therefore, a relatively fast seed value (compared to $k_\gamma$) was used. If it were too slow, there would be significant product inhibition as the steady-state progresses, and this is not seen in the data. Also, Pi release is constrained by the steady-state hydrolysis rate. It has been shown that Pi does not bind productively to the enzyme in the absence of the transport sector $F_O$ and a proton motive force (*23*, *25*, *28*, *30*, *59*); therefore, an arbitrary slow value of 10 $M^{-1}$ $s^{-1}$ was used for the $k_{-3}$ seed value and does not affect progress of the reaction, and in fact, very much smaller values for $k_{-3}$ did not negatively affect the fitting of the model to the data (described further in Sensitivity Analysis below).

(*vi*) The rate of ADP binding, $k_{-4}$, was shown to be rapid from the $\beta$Y331W titration in Figure 4B yet was slower than Mg·ATP binding; therefore, the seed value for $k_{-4}$ was slower than the value of $k_{+1}$. The ratio of $k_{+4}/k_{-4}$ was approximated from experimentally determined affinities. The $K_{I\ ADP}$ was determined under the same conditions (Figure 3B), and the $K_d$ for ADP was calculated from the $\beta$Y331W titration (Figure 4B, and also refs *50* and *53*). Using these data along with the determined $k_{-4}$, a seed value was calculated for the dissociation rate constant $k_{+4}$. These values were consistent with the requirement for a relatively fast rate of ADP release ($k_{+4}$). Similar to Pi, if the release of either product were too slow or rate limiting the steady-state would slow down because of product inhibition. Clearly, ADP release is not rate limiting in the steady-state conditions shown in Figure 1.

(*vii*) It is important to note that the pre-steady-state and the steady-state phases of hydrolysis are fit using the same rate constants. In addition, excellent fits to the data for a wide range of substrate concentrations were achieved with remarkably little variation in the rate constants (Table 1). These two facts emphasize the simplicity of the model and generate a high level of confidence in its validity.

(*viii*) Various alternate models were tested, and the results of the best attainable fits are shown in Figure 5. One stipulation placed on these tests was that the experimentally determined parameters were not allowed to vary to unrealistic values. The 62 $\mu$M Mg·ATP data set was used to fit the alternate models, although other data sets at different Mg·ATP concentrations were also used to validate the results and ensure that the results were not particular to one condition (results not shown). For comparison, the best fit for these data using our model (Scheme 1) is indicated by the solid line in Figure 5.

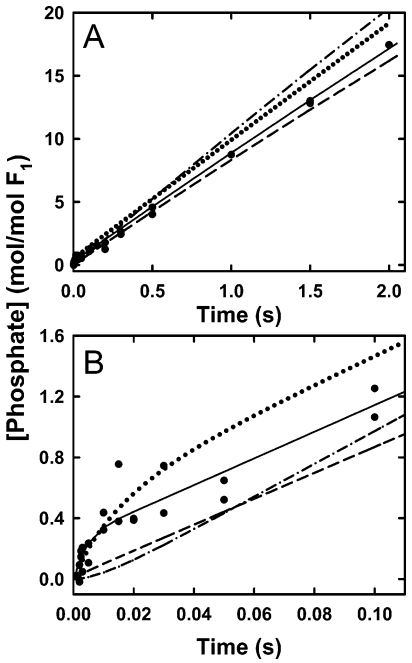


FIGURE 5: Comparison of alternate kinetic models. The data points (●, same as those shown in Figure 1) of the pre-steady-state hydrolysis of $F_1$ at 62 $\mu$M Mg·ATP final concentration are used to attempt fits using alternate kinetic models. (A) The complete time course up to 2.0 s. (B) The early time points up to 0.1 s. The solid line is the best fit for our model using the parameters listed in Table 1 for the 62 $\mu$M Mg·ATP data set (MSC (see Experimental Procedures for definition), 5.56; $R^2$, 0.998). The others lines represent the best fits to alternate models as described in detail in Results. The dashed line (----) is the best fit for a model lacking the rate-limiting step, $k_\gamma$, which is essentially the uni-site model described elsewhere (*25*, *27*) (MSC, 4.40; $R^2$, 0.994). The dot and dashed line (-·-·-) is the best fit for a model where $k_\gamma$ occurs before Step 2, the hydrolysis/synthesis of ATP (MSC, 2.54; $R^2$, 0.964). The dotted line (····) is the best fit for a model where Pi release, $k_{+3}$, occurs before $k_\gamma$ (MSC, 3.03; $R^2$, 0.978).

The first model tested was essentially the uni-site model of catalysis (*25*, *30*), without the rate-limiting step, $k_\gamma$. As can be seen from Figure 5B (----), the model cannot simulate the burst of ATP hydrolysis in the pre-steady state. This emphasizes the need for a rate-limiting step after hydrolysis in the reaction scheme in order to fit the burst. However, if $k_\gamma$ and $k_{+3}$, the release of Pi, are combined in a single rate-limiting step, the burst can be fit, but the steady state is not (result not shown).

The order of $k_\gamma$ within the reaction scheme was also verified using the following two test models: (1) placement of $k_\gamma$ before Step 2, the hydrolysis/synthesis of ATP (-·-·) or (2) placement of $k_\gamma$ after Pi release (····). The first model with $k_\gamma$ before Step 2 also cannot account for the burst of hydrolysis, and there is actually a slight lag evident in the early time course of Pi generated (Figure 5B). The second model with $k_\gamma$ after Pi release can simulate a burst, but the burst is too slow and overshoots the data (Figure 5B). Furthermore, this model fails to fit the steady-state rate (Figure 5A).

We also tested a model where the hydrolysis of ATP is irreversible (no $k_{-2}$), and Pi release, $k_{+3}$, is fast. This possible reaction scheme would imply that the rate-limiting $k_\gamma$ step occurs with hydrolysis of ATP. In this case, the steady-state

rate could be approximated, but the burst could not be fit (result not shown). This result was similar to the model where $k_\gamma$ occurs before the step of chemistry. Our data are thus inconsistent with the model of Weber et al. (*60*), a key element of which is the simultaneous release of phosphate with a $k_{+2}$-driven rotational conformational change.

The fits to a model where the rate-limiting step, $k_\gamma$, is several fold faster than $k_{-\gamma}$ were of good quality; however, the model where $k_\gamma$ is essentially irreversible achieved the best fit (Figure 5A and B (—); $R^2 = 0.998$; MSC = 5.56). In comparison, the quality of the fit where $k_\gamma$ and $k_{-\gamma}$ were constrained to equal values was much worse (MSC = 3.03; data not shown), and when $k_{-\gamma}$ was large compared with $k_\gamma$ (e.g., 4-fold greater), the model fit to the data was very poor (MSC = 1.56) and resulted in pre-steady-state and steady-state rates that were far too slow. Although $k_\gamma$ may not be irreversible, these analyses show that the reverse rate is much smaller than the forward reaction. This conclusion is consistent with the observations of single molecule behavior, where the rotor very rarely takes a backward step (*61*, *62*).

In summary, a minimal number of partial reactions provide an excellent fit to the pre-steady-state and steady-state data. We emphasize that the order of the partial reaction steps shown in Scheme 1 is a unique solution to all of the data and is consistent with observations in the literature.

*Sensitivity Analysis.* The sensitivity of each of the rate constants was determined (as described in Experimental Procedures) as a means to analyze which constants are important for fitting the model to the data and determining the rate of the reaction. Each of the constants was perturbed, one at a time (except where noted), and the new set of parameters was refined using the simplex technique to locate a region of minima. Following the parameter refinement, the nonlinear least-squares minimization algorithm was performed to finalize the model fit. The fit was analyzed statistically to determine the MSC value, which is the most sensitive way to evaluate the goodness-of-fit of the model using the new parameter set. Although an infrequent occurrence, model fits to the data that changed experimentally verified parameters to unrealistic values were considered bad fits.

Table 2 shows the results of the analysis. A 10-fold increase or decrease of each parameter individually, up to and including the rate-limiting step ($k_\gamma$), was a perturbation not tolerated by the model. A change of 10-fold of those rate constants occurring after the rate-limiting step in the reaction was not as detrimental to achieving a fit, although the quality of the fits were substantially decreased. The exception was $k_{-3}$, Pi binding, which was almost unaffected. This is consistent with previous studies that show Pi does not bind in a productive manner in the absence of a proton motive force and the $F_O$ sector, that is, that Pi release is essentially an irreversible reaction in the hydrolysis mode. A 10-fold increase or decrease of $k_{+2}$ and $k_{-2}$ together, thus retaining the ratio between ATP hydrolysis and synthesis, failed to fit. Although the change in the $k_{+2}$ and $k_{-2}$ rates was more sensitive than any of the other constants occurring after $k_\gamma$, it was not as sensitive as forcing the ATP hydrolysis/synthesis ratio, $K_2$, away from unity.

In order to establish a more rigorous criterion for sensitivity, the analysis was performed once more, but with a 2-fold increase or decrease of the parameter values. Similar to the 10-fold perturbations, the parameters leading up to and including $k_\gamma$ were very sensitive to perturbation. The parameters after the rate-limiting step were almost insensitive to the 2-fold perturbation, with the exception of $k_{+3}$, Pi release. This shows that the rate of Pi release does affect the rate of the reaction.

The fact that the rate constants up to $k_\gamma$ were more sensitive than those after this step gives credence to the fact that $k_\gamma$ is the rate-limiting step and emphasizes that its order in the reaction is critical. Significantly, it has the smallest window within which its value can accurately describe the data. Overall, even the relatively non-sensitive parameters do not tolerate a 10-fold change, which in enzymatic terms is relatively small. The more sensitive parameters (those occurring before and including $k_\gamma$) do not tolerate even a 2-fold change in the rates, thus giving us a high level of confidence in our model.

## DISCUSSION

The pre-steady-state kinetics of ATP binding and hydrolysis of the $F_1$-ATPase in the rotational catalytic mode have been determined for the first time. A high concentration of Mg·ATP was used to start the reaction in order to fill all three catalytic sites, which was required to achieve full promotion of ATP hydrolytic activity and to efficiently couple $\gamma$ subunit rotation to hydrolysis for the reasons already outlined in the Introduction. Experimental results from several laboratories were taken together to conclude that Mg·ATP was required at high enough concentration ($>10^{-5}$ M) to occupy the low affinity site in order for the enzyme to enter a cooperative rotational catalytic mode. The data clearly showed that upon rapid mixing of the enzyme with high concentrations of Mg·ATP, it *immediately* entered into a rotational catalysis mode.

In multisite catalysis, all of the rate constants are much faster than those determined for uni-site conditions, and an additional rate-limiting step must be added, which comes prior to Pi and ADP release (see Results and refs *25*, *27*, *58*, and *63*). The faster rate constants necessitated the use of millisecond mixing, which was apparent from the time course of hydrolysis shown in Figure 1B and C. Resolution of the burst of ATP hydrolysis provided constraints that were critical in defining the kinetic model and rate constants of the partial reactions. Importantly, the same kinetic model and rate constants could be used to fit and simulate both pre-steady state and steady-state phases accurately. *Thus, we found that it was valid to use the pre-steady-state rate constants to describe partial reaction rates in the steady state.* A variety of models were tested systematically, and a unique solution was found that was able to fit all of the data from a wide range of substrate concentrations. Furthermore, the kinetic model presented in this article is consistent with important properties of the enzyme characterized in previous publications (reviewed in ref *2*).

Several lines of evidence indicate that Mg·ADP inhibition is not observed in the pre-steady-state hydrolysis data presented here. First, the active site titration of the pre-steady-state burst shows that the enzyme is essentially 100% active with one site per $F_1$ molecule carrying out reversible hydrolysis/synthesis of ATP immediately after rapid mixing with the substrate. Second, the kinetics of the longer steady-

state hand-mixing measurements were the same as the steady-state kinetics of the rapid-mixing experiments. The data could not be fit if the rate constant for ADP release was slower, as shown by the sensitivity analysis. Finally, a single set of rate constants would not be adequate to describe both the pre-steady-state and steady-state data if there was a conversion between the Mg·ADP-inhibited and -uninhibited forms of the enzyme.

The experimentally demonstrated reaction sequence and kinetic rate constants were incorporated into a rotational catalytic model shown in graphical form in Figure 6. Although the same rate constants were used to describe both the pre-steady state and the steady state, the first cycle is presented separately from the subsequent steady-state cycles because two ATP and one ADP are bound rather than the one ATP and two ADP + Pi bound in the steady-state mode (see below). Rapid addition of Mg·ATP to the enzyme shows that the substrate associates with all three sites in a diffusion-limited manner (Figure 4). Binding of the higher Mg·ATP concentrations to the catalytic sites of the $\beta$Y331W enzyme in the fluorescence stopped-flow traces shows that the initial binding is completed within the 1 ms dead time of the instrument. This is faster than the calculated rate constant for binding, $k_{+1}$, determined from the model fits (see Table 1).

The slightly slower than expected $k_{+1}$ probably reflects the partial rotation that takes place to put $\beta_{TP}$ in a state that undergoes reversible hydrolysis/synthesis. Previous kinetic analysis of the submillisecond rotational behavior of single molecules resolved a brief pause in $\gamma$ subunit rotation that defined two partial rotation steps (*24*, *64*). The first substep, corresponding to the 80° rotation (*64*), occurred in an ATP dependent manner and was assigned to ATP binding. In the pre-steady-state cycle (shown in the top two rows of Figure 6), we hypothesize a sequential cooperative binding of ATP. In our model, ATP binding to the third site, $\beta_E$, drives the partial 80° $\gamma$ subunit rotation and forces the change of the $\beta_E$ conformer (red) into the half-closed ($\beta_{HC}$, purple) conformer, which was structurally observed by Menz et al. (*65*) and incorporated into a catalytic model by Senior et al. (*4*). In the hydrolysis direction, this partial rotation is not a rate-limiting step, but it activates the $\beta_{TP}$ site by putting it in a conformation that can carry out reversible hydrolysis/synthesis, $k_{+2}/k_{-2}$. The similar value for the $K_d$ of Mg·ATP binding to the low affinity site and the $K_M$ for the extent of the burst of Mg·ATP hydrolysis (Figures 1 and 2) support this notion, as does the fact that ATP hydrolysis is clearly not rate limiting to the reaction (Figure 1B and C, and Table 1). In addition, the ratio of ATP hydrolysis/synthesis rates ($K_2$) at the active site was found to be close to unity in the rotational catalytic mode, similar to the uni-site mode of the enzyme, and consistent with the binding change mechanism of Boyer (*66*, *67*). In the synthesis direction, we hypothesize that the partial rotation is the energy-requiring step that changes the conformational state from $\beta_{TP}$ to $\beta_E$, thus decreasing the affinity for ATP and allowing its release from the enzyme (*58*).

We needed to add a kinetic step, $k_\gamma$, to account for the burst of ATP hydrolysis. Moreover, to simulate both the pre-steady state and steady-state phases of the data, $k_\gamma$ must follow hydrolysis and precede the release of Pi, $k_{+3}$. Models in which $k_\gamma$ and $k_{+3}$ were combined into the same step, $k_{+3}$ preceded $k_\gamma$, or $k_{+3}$ was much faster, failed to give satisfactory fits to either the pre-steady-state or steady-state phases. Consistent with this conclusion, Masaike et al. (*68*) detected an ATP-dependent fluorescence intensity change of a tryptophan near the catalytic site, which indicated a conformational shift. The fluorescence changed with a rate slower than that of nucleotide binding but occurred with the same kinetics as that of Pi release. Previously, we presented an extensive Arrhenius analysis of steady-state data of the $\gamma$Met23 to Lys mutant enzyme, which perturbed the interactions between the stator $\beta$ and rotor $\gamma$ subunits (*58*). Our results suggested that the rate-limiting transition state occurred during $\gamma$ subunit rotation between hydrolysis and release of Pi, and we now present pre-steady-state kinetic data that show that the conformational change must occur after hydrolysis. Taken together, it is clear that the rate-limiting transition state occurs during the 40° partial rotation observed by Shimbakuro et al. (*64*), which we now call $k_\gamma$. It is likely that $k_\gamma$ involves several partial reactions, but the chemical approach used in this article cannot distinguish these steps, and modeling the step as a single rate constant is sufficient for the purposes of fitting the kinetic data.

Furthermore, the data presented show that $k_\gamma$ and Pi release are essentially irreversible because it is likely that they are the major energy-producing steps of the hydrolysis pathway. This is in agreement with experimental evidence in the synthesis direction, where an input of energy from the proton motive force is required for Pi binding (*58*). This is also in agreement with the rotational behavior of $F_1$, which is observed not to reverse the direction of rotation in the presence of high Mg·ATP concentrations (*61*, *69*). The model indicates that $\gamma$ subunit rotation, in the direction of hydrolysis, drives the conformational change, which leads to a decrease in affinity for Pi and converts the $\beta_{DP}$ conformation to $\beta_E$, allowing the release of products. Depicted in the first cycle of the model (Figure 6, asterisk at the first $k_{+3}$), there is no Pi released because of $\gamma$ rotation because there is no Pi in the $\beta_{DP}$ site from a previous cycle of hydrolysis. Mg·ATP binds to the newly vacated $\beta_E$ to trigger the next round of hydrolysis. We also note that product release, either Pi or ADP, cannot be rate limiting, otherwise a product bound form of the enzyme would accumulate during the steady state, slowing down the steady-state rate.

One catalytically competent site is expected on the basis of the many uni-site studies that have unequivocally established that a catalytically active, high affinity site is available for ATP binding and hydrolysis. In the pre-steady state and steady state, our data (Figure 1) show that only one site is hydrolyzing ATP per cycle. However, earlier reports have hinted that a second site is catalytically competent. A second site was implied by the X-ray crystallographic structure of bovine $F_1$ obtained in the presence of ADP and $AlF_4^-$ by Menz et al. (*65*). In this structure, the two catalytic sites in the $\beta_{TP}$ and $\beta_{DP}$ subunits had very similar conformations, and both had ADP·$AlF_4^-$ bound. Similarly, Nadanaciva et al. (*70*) found that two of the *E. coli* $F_1$ catalytic sites could attain transition state conformations using Mg·ADP plus fluoroscandium. In addition, Weber et al. (*71*), using the $\beta$F148W mutant, whose fluorescence differentiates between bound ADP and ATP, found one mole of ATP and two moles of ADP were bound in conditions of maximal ATPase rates. The only model consistent with all of these results is that

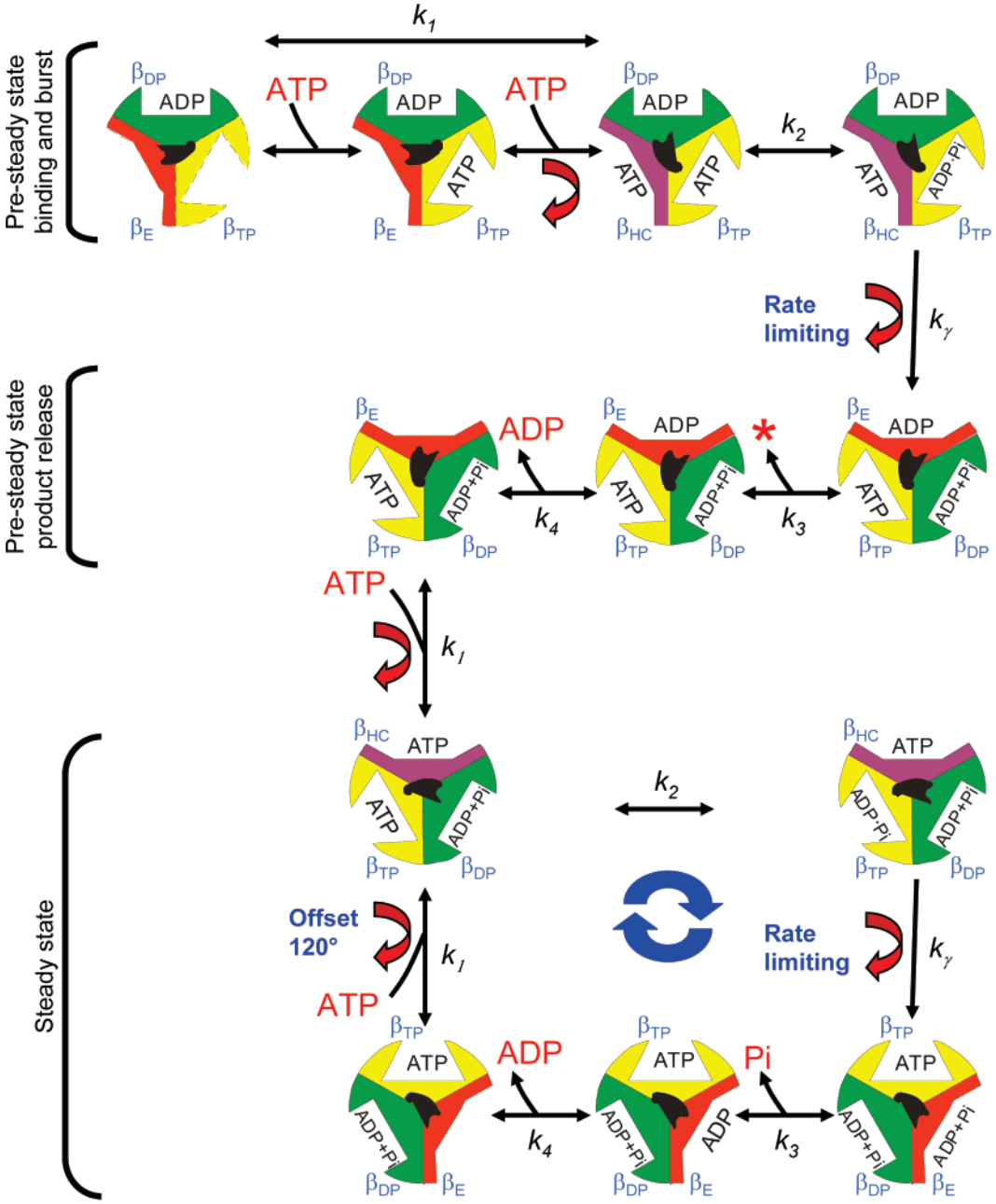


FIGURE 6: Graphical representation of the rotational catalytic pathway from pre-steady state into steady-state hydrolysis. The three site rotational reaction scheme is depicted for the $F_1$ enzyme in the hydrolysis mode of catalysis. The model is discussed in detail in the text. The relative arrangement of the $\beta$ subunit conformations are as viewed from the top of the complex toward the membrane. The three site conformations, $\beta_{DP}$ (green), $\beta_{TP}$ (yellow), and $\beta_E$ (red) are as presented by Abrahams et al. (*8*), and $\beta_{HC}$ (purple) refers to the half-closed intermediate conformation structure described by Menz et al. (*65*) and incorporated into a mechanistic model of $F_1$ rotational catalysis by others (e.g., Senior et al.; ref *4*). In the starting conformation (upper left), the exact conformation of the initial state of the enzyme is rather ambiguous; therefore, dashed lines are used to indicate the likely conformations. The noncatalytic α subunits are omitted for clarity. The central asymmetric shape represents the position of the $\gamma$ subunit during the course of catalysis. The intermediate rotation of 80° and the completion of rotation to the next 120° position correspond to the observed dwell positions (*24*, *64*). The brackets on the left indicate the mode of kinetics corresponding to the data presented in this article. The steps of the first cycle responsible for the pre-steady-state kinetics are represented by the top two rows. The burst of hydrolysis occurs through the relatively rapid binding step ($k_{+1}$) to the step of chemistry ($k_{+2}$). The binding of two ATP to $\beta_{TP}$ and $\beta_E$ only occurs in the first turnover, and the asterisk for the first $k_{+3}$ indicates that there is no Pi to release in the pre-steady state. In the steady state (surrounding the circular blue arrows in the third and fourth rows), only one ATP binds per cycle to the $\beta_E$ site. We also note that the $\beta_{TP}$ site does not hydrolyze bound ATP unless ATP is also bound to the $\beta_E$ site, thus converting it to the $\beta_{HC}$ conformation (between $k_1$ and $k_2$). The position of the $\gamma$ subunit is offset 120° for each cycle in the steady-state mode of the enzyme. The rate-limiting transition state for pre- and steady-state catalysis as described in Al-Shawi et al. (*58*) and Nakamoto et al. (*2*) occurs during the $k_\gamma$ rotation step.

one site is in the process of hydrolyzing ATP and the other is holding ADP + Pi that was produced in the previous cycle. In this case, $\beta_{TP}$ must be the site of catalysis. This conclusion is in contrast to other models including those of Menz et al. (*65*) and Senior et al. (*4*) that suggest that $\beta_{DP}$ is the site of chemistry. Such models do not account for the cooperativity of the three sites or the average occupancy of the sites, almost three, in steady-state conditions (*23*). The sequence order of $\beta$ subunit conformations through a rotation cycle in the direction of hydrolysis is $\beta_E$-$\beta_{HC}$-$\beta_{TP}$-$\beta_{DP}$; therefore, the site

of catalysis cannot be $\beta_{DP}$; otherwise, there would be two sites containing ATP and one site with ADP. It was previously hypothesized that site $\beta_{DP}$ also has bound Pi on the basis of the apparent positive cooperativity of phosphate in the activation of ATP synthesis (*58*). ATP synthesis has a sigmoidal dependence upon Pi concentration with a Hill coefficient close to 2, suggesting that there are two molecules of Pi bound during steady-state ATP synthesis. We hypothesized earlier that the conserved and essential amino acid αArg376 (*22*) plays the critical role of retaining product Pi in the catalytic site until it is released as the $\beta_{DP}$ is converting to the $\beta_E$ site. These results suggest that Pi is released from $\beta_{DP}$; therefore, it follows that Pi is not released until the cycle after which it was produced. In this manner, we suggest that the enzyme is able to utilize the binding energy of Pi to maintain efficient coupling between catalysis and rotation.

The order of the partial reactions presented above provides us with a framework to understand how $F_1$-ATPase maintains coupling between catalysis and rotation. The enzyme requires that the rate-limiting step, $k_\gamma$, occurs after the reversible hydrolysis/synthesis reaction and prior to Pi release. Clearly, if Pi is released without coupling to rotation, coupling efficiency decreases. This is the case with the replacement of the conserved $\gamma$ subunit Met23 with Lys. The mutant enzyme allows a pathway where Pi can be released without rotation (*58*). This same mutant enzyme also had a higher $K_M$ for Pi in ATP synthesis, which implied that the perturbation of the interaction between $\gamma$ and $\beta$ subunits blocked the ability of the catalytic site to achieve the proper conformation for binding Pi. Furthermore, an Arrhenius analysis of the mutant enzyme showed that the amino acid replacement directly affected the rate-limiting transition state of steady-state ATP hydrolysis (*15*). Taken together, our analyses show that the $F_1$ enzyme maintains efficient coupling by requiring that Pi can only be released after the rate-limiting 40° rotation step, $k_\gamma$.

## ACKNOWLEDGMENT

We thank Julie Teater and Dorothy Zhang for excellent technical assistance.

## REFERENCES

1. Nakamoto, R. K. (1999) Molecular features of energy coupling in the $F_OF_1$ ATP Synthase, *News Physiol. Sci. 14*, 40−46.
2. Nakamoto, R. K., Ketchum, C. J., and Al-Shawi, M. K. (1999) Rotational coupling in the $F_OF_1$ ATP synthase, *Annu. Rev. Biophys. Biomol. Struct. 28*, 205−234.
3. Ren, H., and Allison, W. S. (2000) On what makes the $\gamma$ subunit spin during ATP hydrolysis by $F_1$, *Biochim. Biophys. Acta 1458*, 221−233.
4. Senior, A. E., Nadanaciva, S., and Weber, J. (2002) The molecular mechanism of ATP synthesis by $F_1F_O$-ATP synthase, *Biochim. Biophys. Acta 1553*, 188−211.
5. Boyer, P. D. (2002) Catalytic site occupancy during ATP synthase catalysis, *FEBS Lett. 512*, 29−32.
6. Kinosita, K., Adachi, K., and Itoh, H. (2004) Rotation of $F_1$-ATPase: how an ATP-driven molecular machine may work, *Annu. Rev. Biophys. Biomol. Struct. 33*, 245−268.
7. Dittrich, M., and Schulten, K. (2005) Zooming in on ATP hydrolysis in $F_1$, *J. Bioenerg. Biomembr. 37*, 441−444.
8. Abrahams, J. P., Leslie, A. G. W., Lutter, R., and Walker, J. E. (1994) Structure at 2.8 Å resolution of $F_1$-ATPase from bovine heart mitochondria, *Nature 370*, 621−628.
9. Aggeler, R., Cai, S. X., Keana, J. F. W., Koike, T., and Capaldi, R. A. (1993) The $\gamma$ subunit of the *Escherichia coli* $F_1$-ATPase can be cross-linked near the glycine-rich loop region of a $\beta$ subunit when ADP+$Mg^{2+}$ occupies catalytic sites but not when ATP+$Mg^{2+}$ is bound, *J. Biol. Chem. 268*, 20831−20837.
10. Aggeler, R., and Capaldi, R. A. (1996) Nucleotide-dependent movement of the $\epsilon$ subunit between α and $\beta$ subunits in the *Escherichia coli* $F_1F_O$-type ATPase, *J. Biol. Chem. 271*, 13888−13891.
11. Aggeler, R., Haughton, M. A., and Capaldi, R. A. (1995) Disulfide bond formation between the COOH-terminal domain of the $\beta$ subunits and the $\gamma$ and $\epsilon$ subunits of the *Escherichia coli* $F_1$-ATPase, *J. Biol. Chem. 270*, 9185−9191.
12. Duncan, T. M., Bulygin, V. V., Zhou, Y., Hutcheon, M. L., and Cross, R. L. (1995) Rotation of subunits during catalysis by *Escherichia coli* $F_1$-ATPase, *Proc. Natl. Acad. Sci. U.S.A. 92*, 10964−10968.
13. Aggeler, R., Grüber, G., and Capaldi, R. A. (1998) Trapping of conformations of the *Escherichia coli* $F_1$ ATPase by disulfide bond formation, *FEBS Lett. 426*, 37−40.
14. Tsunoda, S. P., Muneyuki, E., Amano, Y., Yoshida, M., and Noji, H. (1999) Cross-linking of two $\beta$ subunits in the closed conformation in $F_1$-ATPase, *J. Biol. Chem. 274*, 5701−5706.
15. Al-Shawi, M. K., Ketchum, C. J., and Nakamoto, R. K. (1997) Energy coupling, turnover, and stability of the $F_OF_1$ ATP synthase are dependent on the energy of interaction between $\gamma$ and $\beta$ subunits, *J. Biol. Chem. 272*, 2300−2306.
16. Nakamoto, R. K., Al-Shawi, M. K., and Futai, M. (1995) The ATP synthase $\gamma$ subunit: suppressor mutagenesis reveals three helical regions involved in energy coupling, *J. Biol. Chem. 270*, 14042−14046.
17. Nakamoto, R. K., Maeda, M., and Futai, M. (1993) The $\gamma$ subunit of the *Escherichia coli* ATP synthase: mutations in the carboxyl-terminal region restore energy coupling to the amino-terminal mutant, $\gamma$Met-23→Lys, *J. Biol. Chem. 268*, 867−872.
18. Rao, R., Perlin, D. S., and Senior, A. E. (1987) The defective proton-ATPase of *uncA* mutants of *Escherichia coli*: ATP-binding and ATP-induced conformational change in mutant α-subunits, *Arch. Biochem. Biophys. 255*, 309−315.
19. Maggio, M. B., Pagan, J., Parsonage, D., Hatch, L., and Senior, A. E. (1987) The defective proton-ATPase of *uncA* mutants of *Escherichia coli*: identification by DNA sequencing of residues in the α-subunit which are essential for catalysis or normal assembly, *J. Biol. Chem. 262*, 8981−8984.
20. Weber, J., Bowman, C., Wilke-Mounts, S., and Senior, A. E. (1995) α-Aspartate 261 is a key residue in noncatalytic sites of *Escherichia coli* $F_1$-ATPase, *J. Biol. Chem. 270*, 21045−21049.
21. Nadanaciva, S., Weber, J., Wilke-Mounts, S., and Senior, A. E. (1999) Importance of $F_1$-ATPase residue α-Arg-376 for catalytic transition state stabilization, *Biochemistry 38*, 15493−15499.
22. Le, N. P., Omote, H., Wada, Y., Al-Shawi, M. K., Nakamoto, R. K., and Futai, M. (2000) The *Escherichia coli* ATP synthase α subunit Arg-376: the catalytic site arginine does not participate in the hydrolysis/synthesis reaction but is required for promotion to steady state, *Biochemistry 39*, 2778−2783.
23. Weber, J., Wilke-Mounts, S., Lee, R. S.-F., Grell, E., and Senior, A. E. (1993) Specific placement of tryptophan in the catalytic sites of *Escherichia coli* $F_1$-ATPase provides a direct probe of nucleotide binding: maximal ATP hydrolysis occurs with three sites occupied, *J. Biol. Chem. 268*, 20126−20133.
24. Yasuda, R., Noji, H., Yoshida, M., Kinosita, K., and Itoh, H. (2001) Resolution of distinct rotational substeps by submillisecond kinetic analysis of $F_1$-ATPase, *Nature 410*, 898−904.
25. Grubmeyer, C., Cross, R. L., and Penefsky, H. S. (1982) Mechanism of ATP hydrolysis by beef-heart mitochondrial ATPase: rate constants for elementary steps in catalysis at a single site, *J. Biol. Chem. 257*, 12092−12100.
26. Cross, R. L., Grubmeyer, C., and Penefsky, H. S. (1982) Mechanism of ATP hydrolysis by beef heart mitochondrial ATPase: rate enhancements resulting from cooperative interactions between multiple catalytic sites, *J. Biol. Chem. 257*, 12101−12105.
27. Duncan, T. M., and Senior, A. E. (1985) The defective proton-ATPase of *uncD* mutations of *Escherichia coli*: two mutations which affect the catalytic mechanism, *J. Biol. Chem. 260*, 4901−4907.
28. Al-Shawi, M. K., and Senior, A. E. (1988) Complete kinetic and thermodynamic characterization of the unisite catalytic pathway of *Escherichia coli* $F_1$-ATPase, *J. Biol. Chem. 263*, 19640−19648.
29. García, J. J., and Capaldi, R. A. (1998) Unisite catalysis without rotation of the $\gamma$-$\epsilon$ domain in *Escherichia coli* $F_1$-ATPase, *J. Biol. Chem. 273*, 15940−15945.

30. Al-Shawi, M. K., and Senior, A. E. (1992) Catalytic sites of *Escherichia coli* $F_1$-ATPase. Characterization of unisite catalysis at varied pH, *Biochemistry 31*, 878−885.
31. Klionsky, D. J., Brusilow, W. S. A., and Simoni, R. D. (1984) *In vivo* evidence for the role of the $\epsilon$ subunit as an inhibitor of the proton-translocating ATPase of *Escherichia coli*, *J. Bacteriol. 160*, 1055−1060.
32. Moriyama, Y., Iwamoto, A., Hanada, H., Maeda, M., and Futai, M. (1991) One-step purification of *Escherichia coli* $H^+$-ATPase ($F_oF_1$) and its reconstitution into liposomes with neurotransmitter transporters, *J. Biol. Chem. 266*, 22141−22146.
33. Andrews, S. H., Peskova, Y. B., Polar, M. K., Herlihy, V. B., and Nakamoto, R. K. (2001) Conformation of the $\gamma$ subunit at the $\gamma$-$\epsilon$-c interface in a complete *Escherichia coli* $F_1$-ATPase complex by site-directed spin labeling, *Biochemistry 40*, 10664−10670.
34. Penefsky, H. S. (1979) A centrifuged-column procedure for the measurement of ligand binding by beef heart $F_1$, *Methods Enzymol. 56*, 527−530.
35. Lowry, O. H., Rosebrough, N. J., Farr, A. C., and Randall, R. J. (1951) Protein measurement with the folin phenol reagent, *J. Biol. Chem. 193*, 265−275.
36. Kimura, Y., Shibasaki, S., Morisato, K., Ishizuka, N., Minakuchi, H., Nakanishi, K., Matsuo, M., Amachi, T., Ueda, M., and Ueda, K. (2004) Microanalysis for MDR1 ATPase by high-performance liquid chromatography with a titanium dioxide column, *Anal. Biochem. 326*, 262−266.
37. Froehlich, J. P., Sullivan, J. V., and Berger, R. L. (1976) A chemical quenching apparatus for studying rapid reactions, *Anal. Biochem. 73*, 331−341.
38. Sugino, Y., and Miyoshi, Y. (1964) The specific precipitation of orthophosphate and some biochemical applications, *J. Biol. Chem. 239*, 2360−2364.
39. Ray, M. K., Connerton, I. F., and Griffiths, D. E. (1988) DNA sequence analysis of the *Oli$^r$ 2-76* and *Oss$^r$ 1-92* alleles of the *Oli-2* region of the yeast *Saccharomyces cerevisiae*. Analysis of related amino acid substitutions and protein antibiotic interaction, *Biochim. Biophys. Acta 951*, 213−219.
40. Deming, S. N., and Morgan, S. L. (1979) The use of linear models and matrix least squares in clinical chemistry, *Clin. Chem. 25*, 840−855.
41. Powell, M. J. D. (1970) *A FORTRAN Subroutine for Solving Systems of Nonlinear Algebraic Equations*, Gordan & Breach Science Publishers, New York, NY.
42. MicroMath Research (1995) *MicroMath Scientist: for Experimental Data Fitting/Microsoft Windows*, Version 2.0, MicroMath Research, St. Louis, MO.
43. Akaike, H. (1974) A new look at the statistical model identification, *IEEE Trans. Autom. Control 19*, 716−723.
44. Akaike, H. (1976) What is Akaike information criterion, *Math. Sci. (Tokyo) 14*, 5−11.
45. Fabiato, A., and Fabiato, F. (1979) Calculator programs for computing the composition of the solutions containing multiple metals and ligands used for experiments in skinned muscle cells, *J. Physiol. (Paris) 75*, 463−505.
46. Al-Shawi, M. K., Parsonage, D., and Senior, A. E. (1988) Directed mutagenesis of the strongly conserved aspartate 242 in the $\beta$-Subunit of *Escherichia coli* proton-ATPase, *J. Biol. Chem. 263*, 19633−19639.
47. Wise, J. G., Latchney, L. R., and Senior, A. E. (1981) The defective proton-ATPase of *uncA* mutants of *Escherichia coli*: studies of nucleotide binding sites, bound aurovertin fluorescence, and labeling of essential residues of the purified $F_1$-ATPase, *J. Biol. Chem. 256*, 10383−10389.
48. Nalin, C. M., and Cross, R. L. (1982) Adenine nucleotide binding sites on beef-heart $F_1$-ATPase: specificity of cooperative interactions, *J. Biol. Chem. 257*, 8055−8060.
49. Cross, R. L., and Nalin, C. M. (1982) Adenine nucleotide binding sites on beef heart $F_1$-ATPase: evidence for three exchangeable sites that are distinct from three noncatalytic sites, *J. Biol. Chem. 257*, 2874−2881.
50. Weber, J., and Senior, A. E. (2001) Bi-site catalysis in $F_1$-ATPase: does it exist, *J. Biol. Chem. 276*, 35422−35428.
51. Senior, A. E., Lee, R. S.-F., Al-Shawi, M. K., and Weber, J. (1992) Catalytic properties of *Escherichia coli* $F_1$-ATPase depleted of endogenous nucleotides, *Arch. Biochem. Biophys. 297*, 340−344.
52. Senior, A. E., and Al-Shawi, M. K. (1992) Further examination of seventeen mutations in *Escherichia coli* $F_1$-ATPase $\beta$-subunit, *J. Biol. Chem. 267*, 21471−21478.
53. Löbau, S., Weber, J., Wilke-Mounts, S., and Senior, A. E. (1997) $F_1$-ATPase, roles of three catalytic site residues, *J. Biol. Chem. 272*, 3648−3656.
54. Lunardi, J., Dupuis, A., Garin, J., Issartel, J. P., Michel, L., Chabre, M., and Vignais, P. V. (1988) Inhibition of $H^+$-transporting ATPase by formation of a tight nucleoside diphosphate-fluoroaluminate complex at the catalytic site, *Proc. Natl. Acad. Sci. U.S.A. 85*, 8958−8962.
55. Weber, J., and Senior, A. E. (1997) Catalytic mechanism of $F_1$-ATPase, *Biochim. Biophys. Acta 1319*, 19−58.
56. Al-Shawi, M. K., and Nakamoto, R. K. (1997) The mechanism of energy coupling in the $F_OF_1$-ATP synthase: the uncoupling mutation, $\gamma$M23K, disrupts the use of binding energy to drive catalysis, *Biochemistry 36*, 12954−12960.
57. Boyer, P., Cross, R. L., and Momsen, W. (1973) A new concept for energy coupling in oxidative phosphorylation based on a molecular explanation of the oxygen exchange reactions, *Proc. Natl. Acad. Sci. U.S.A. 70*, 2837−2839.
58. Al-Shawi, M. K., Ketchum, C. J., and Nakamoto, R. K. (1997) The *Escherichia coli* $F_OF_1$ $\gamma$M23K uncoupling mutant has a higher $K_{0.5}$ for Pi. Transition state analysis of this mutant and others reveals that synthesis and hydrolysis utilize the same kinetic pathway, *Biochemistry 36*, 12961−12969.
59. Al-Shawi, M. K., Parsonage, D., and Senior, A. E. (1990) Thermodynamic analyses of the catalytic pathway of $F_1$-ATPase from *Escherichia coli*, *J. Biol. Chem. 265*, 4402−4410.
60. Weber, J., Nadanaciva, S., and Senior, A. E. (2000) ATP-driven rotation of the $\gamma$ subunit in $F_1$-ATPase, *FEBS Lett. 483*, 1−5.
61. Yasuda, R., Noji, H., Kinosita, K., and Yoshida, M. (1998) $F_1$-ATPase is a highly efficient molecular motor that rotates with discrete 120° steps, *Cell 93*, 1117−1124.
62. Noji, H., Häsler, K., Junge, W., Kinosita, K., Yoshida, M., and Engelbrecht, S. (1999) Rotation of *Escherichia coli* $F_1$-ATPase, *Biochem. Biophys. Res. Commun. 260*, 597−599.
63. Al-Shawi, M. K., Parsonage, D., and Senior, A. E. (1989) Kinetic characterization of the unisite catalytic pathway of seven $\beta$-subunit mutant $F_1$-ATPases from *Escherichia coli*, *J. Biol. Chem. 264*, 15376−15383.
64. Shimabukuro, K., Yasuda, R., Muneyuki, E., Hara, K. Y., Kinosita, K., and Yoshida, M. (2003) Catalysis and rotation of $F_1$ motor: cleavage of ATP at the catalytic site occurs in 1 ms before 40 degree substep rotation, *Proc. Natl. Acad. Sci. U.S.A. 100*, 14731−14736.
65. Menz, R. I., Walker, J. E., and Leslie, A. G. W. (2001) Structure of bovine mitochondrial $F_1$-ATPase with nucleotide bound to all three catalytic sites: implication for the mechanism of rotary catalysis, *Cell 106*, 331−341.
66. Boyer, P. D. (1975) A model for conformational coupling of membrane potential and proton translocation to ATP synthesis and to active transport, *FEBS Lett. 58*, 1−6.
67. Boyer, P. D. (1993) The binding change mechanism for ATP synthase-some probabilities and possibilities, *Biochim. Biophys. Acta 1140*, 215−250.
68. Masaike, T., Muneyuki, E., Noji, H., Kinosita, K., and Yoshida, M. (2002) $F_1$-ATPase changes its conformations upon phosphate release, *J. Biol. Chem. 277*, 21643−21649.
69. Noji, H., Yasuda, R., Yoshida, M., and Kinosita, K. (1997) Direct observation of the rotation of $F_1$-ATPase, *Nature 386*, 299−302.
70. Nadanaciva, S., Weber, J., and Senior, A. E. (2000) New probes of the F1-ATPase catalytic transition state reveal that two of the three catalytic sites can assume a transition state conformation simultaneously, *Biochemistry 39*, 9583−9590.
71. Weber, J., Bowman, C., and Senior, A. E. (1996) Specific tryptophan substitution in catalytic sites of *Escherichia coli* $F_1$-ATPase allows differentiation between bound substrate ATP and product ADP in steady-state catalysis, *J. Biol. Chem. 271*, 18711−18718.


BI700610M